Ocean Engineering 163 (2018) 583–598

Contents lists available at ScienceDirect

Ocean Engineering

journal homepage: www.elsevier.com/locate/oceaneng

Numerical study of hydrodynamic coefficients of multiple heave plates by large eddy simulations with volume of fluid method

Shining Zhang [a,*], Takeshi Ishihara [b]

[a] Climate Change & Environment Research Division, Economy & Technology Research Institute, Global Energy Interconnection Development and Cooperation Organization, 100031, Beijing, China

[b] Department of Civil Engineering, School of Engineering, The University of Tokyo, 7-3-1 Hongo, Bunkyo-ku, 113-8656, Tokyo, Japan

ARTICLE INFO

Keywords:
Multiple heave plates
Large eddy simulation
Volume of fluid method
Flow pattern
Formulas of hydrodynamic coefficients

ABSTRACT

Hydrodynamic coefficients of multiple heave plates are studied for offshore structures to reduce heave responses in oscillating flows. Large eddy simulations with volume of fluid method are performed to predict the hydrodynamic force on a forced oscillated model with multiple heave plates. Predicted added mass and drag coefficients are validated by a water tank test. Then, flow pattern around the multiple heave plates is investigated to clarify the mechanism of hydrodynamic forces on each plate, and a systematic study on the effects of geometric parameters, such as spacing ratio, diameter ratio and aspect ratio on the hydrodynamics of octagonal heave plate are conducted. Finally, formulas of added mass and drag coefficients for a single and double heave plates with circular, octagonal and square cross-sections are proposed to cover a wide range of application of the heave plate.

1. Introduction

Floating offshore wind turbine (FOWT) is a promising innovation. The world's first full-scale 2.3 MW spar FOWT in Hywind project was installed in Norway by Statoil Hydro in 2009 (Hywind Demo), and the second prototype was the 2 MW semi-submersible FOWT in WindFloat project deployed in Portugal by Principle Power in 2011 (WindFloat). In Japan, a 2 MW spar FOWT in GOTO-FOWT project was built off the coast of Kabashima in 2013 (GOTO FOWT). In addition, another 2 MW semi-submersible FOWT and a 7 MW V-shape semi-submersible FOWT in Fukushima FORWARD project were completed off the coast of Fukushima in 2013 and 2015, respectively (Fukushima FORWARD). In the semi-submersible and advanced spar FOWTs, heave plates are commonly used to reduce heave motions and to shift heave resonance periods out of the first-order wave energy range (Lopez-Pavon and Souto-Iglesias, 2015, Fukushima FORWARD). Some new concepts of floating platform have been adopted. A substation and a 5 MW FOWT constructed in Fukushima FORWARD project (Fukushima FORWARD) adopt an advanced spar consisting of multiple heave plates. The hydrodynamic characteristics of multiple heave plates is one of the key factors for the structural design of platforms.

Morison's equation and potential theory are widely used to predict hydrodynamic loads on the platform of FOWT (Phuc and Ishihara, 2007; Waris and Ishihara, 2012; Jonkman, 2007; Browning et al., 2014; Kvittem et al., 2012). The hydrodynamic coefficients, namely added mass and drag coefficients of heave plates (hereinafter referred to as C_a and C_d, respectively) have to be determined to evaluate hydrodynamic loads on them. The hydrodynamic coefficients of the heave plates can be attained by means of water tank tests (Lopez-Pavon and Souto-Iglesias, 2015; Li et al., 2013), numerical simulations (Lopez-Pavon and Souto-Iglesias, 2015; Tao and Thiagarajan, 2003a, 2003b; Tao et al., 2004, 2007; Tao and Cai, 2004; Garrido-Mendoza et al., 2015; Yang et al., 2014), and empirical formulas (Tao et al., 2007; Tao and Cai, 2004; Philip et al., 2013).

Water tank tests have been carried out intensively to study the hydrodynamic coefficients of circular single heave plate (Lopez-Pavon and Souto-Iglesias, 2015; Tao and Dray, 2008), and square single heave plate (Prislin, Blevins, Halkyard, 1998, Li et al., 2013; An and Faltinsen, 2013; Prislin, Blevins, Halkyard, 1998; Wadhwa and Thiagarajan, 2009). Hydrodynamic coefficients of circular and square single heave plates were compared between each other in the study by Lopez-Pavon and Souto-Iglesias (2015). They pointed out that both C_a and C_d of the square heave plate are smaller than those of the circular heave plate. They also confirmed that there is a relatively weak dependence of oscillating frequencies, and a large dependence with Keulegan-Carpenter (KC) number, as well documented in references (Li et al., 2013; An and Faltinsen,

* Corresponding author.
E-mail address: shining-zhang@geidco.org (S. Zhang).

https://doi.org/10.1016/j.oceaneng.2018.03.060
Received 14 November 2016; Received in revised form 12 February 2018; Accepted 21 March 2018

2013). Wadhwa et al. (Wadhwa and Thiagarajan, 2009; Wadhwa et al., 2010) investigated the hydrodynamic coefficients of a heave plate near the free surface. As the submergence of the heave plate decreases, the free surface is expected to be disturbed. It was observed that both C_a and C_d continuously increase as the distance to the free surface increases. Li et al. (2013) studied the influence of plates spacing on the hydrodynamic coefficients. It was found that the hydrodynamic coefficients decrease as spacing decreases.

A number of numerical studies on the hydrodynamic characteristics of heave plate have been conducted. Tao and Cai (2004) investigated influences of heave plate diameter and KC number on hydrodynamic coefficients by finite difference method. Predicted damping ratio agreed well with the measured ones in both low and high KC regimes. Tao and Thiagarajan, 2003a, 2003b presented three vortex shedding modes for oscillating heave plate and proposed a quantitative method of identifying the vortex shedding flow regimes. Lopez-Pavon and Souto-Iglesias (2015) performed a numerical analysis of the hydrodynamic performance of heave plate by a finite volume method with Shear Stress Transport (SST) turbulent model. The accuracy of the computations was found reasonable for a plain plate, while some errors were found for a reinforced plate. Holmes et al. (2001) examined the hydrodynamic coefficients of a square heave plate by a finite element method with LES turbulent model. It was observed that the predicted force by Morison's equation with determined hydrodynamic coefficients matched well with the measured force, even in random wave conditions. Tao et al. (2007) investigated spacing effects on the hydrodynamics of double circular heave plates, and provided a recommendation for the arrangement of adjacent heave plate. However, in these studies, hydrodynamic coefficients of the double heave plates were not validated by water tank tests, and mechanism of hydrodynamic force on multiple heave plates has not been clarified yet.

Formulas are beneficial for optimizing the design of offshore structures with heave plates. The added mass of a pure circular heave plate along its axis approximately equals to the mass of a sphere of water enclosing the heave plate (Sarpkaya, 2010). Tao and Cai (2004) proposed a formula for added mass of a circular heave plate attached by a column. A formula for double circular heave plates by considering the effect of spacing ratio is firstly proposed by Tao et al. (2007), and the predicted added mass coefficient matches well with that obtained from the numerical simulation at low KC number. Philip (Philip et al., 2013) put forward a simplified formula for added mass of a vertical cylinder with multiple heave plates. However, the formula is only suitable for non-interacting plates, which indicates the effect of heave plate spacing is not considered. All the proposed formulas are limited to circular heave plates, and influence of KC number is not taken into account. In contrast to the formulas of C_a, the formula of C_d is seldom studied. Tao and Thiagarajan (2003a) identified the coefficients in the formulas of C_d proposed by Graham (1980) for each defined vortex shedding flow regime, but it might be inappropriate to propose the piecewise formula of C_d since there are no clear watersheds to distinguish the vortex shedding regimes. Therefore, a formula of C_d covering those wide ranges of vortex shedding regime is preferred. Formulas of both C_a and C_d are also expected to cover various cross-sections of heave plates, such as circular, octagonal and square heave plate, and geometric parameters, such as aspect ratio, diameter ratio, and spacing ratio.

In this paper, section 2 describes governing equations and volume of fluid method, grid arrangement, boundary conditions, cases of simulations, and provides the validation of numerical results by a water tank test. Section 3 clarifies the mechanism of hydrodynamic forces on multiple heave plate, and investigates the effect of geometrical parameters, such as spacing ratio, diameter ratio, and aspect ratio. In Section 4, formulas of C_a and C_d for a single and double heave plates are proposed, and the accuracy of hydrodynamic coefficients predicted by proposed formulas is validated by published data in literature and present numerical simulations. The conclusions are summarized in Section 5.

2. Numerical model and validation

In this section, numerical model of a floater with multiple heave plates is introduced, which is a 1/100 down-scaled Froude model of a substation (Yoshimoto, 2016) employed in Fukushima FORWARD project. The floater contains three hulls, which are connected by one cylindrical column. The fully submerged middle and lower hull have the function of heave plate in reducing heave motion. The overview of the floater and its dimensions are shown in Fig. 1. The center line of the upper hull is located at still water level (SWL). All the hulls are octagonal cross-sectional plate. The detailed dimension of the model is specified in Table 1.

The governing equation and VOF method is given in section 2.1. The computational domain and grid arrangement are described in section 2.2. Section 2.3 presents the numerical schemes and boundary conditions. Cases conducted in this study are shown in section 2.4. The definition of the hydrodynamic coefficients is provided in section 2.5. The description of water tank test and validation of numerical results are given in section 2.6 and 2.7, respectively.

2.1. Governing equation

Large-eddy simulation (LES) is adopted and the Boussinesq hypothesis is employed, and the standard Smagorinsky-Lilly model is used to calculate the subgrid-scale (SGS) stresses. The governing equations in Cartesian coordinates are expressed in the form of tensor as Eq. (1) and Eq. (2).

$$\frac{\partial \tilde{u}_i}{\partial x_i} = 0 \tag{1}$$

$$\rho\frac{\partial \tilde{u}_i}{\partial t} + \rho\frac{\partial \tilde{u}_i\tilde{u}_j}{\partial x_j} = -\frac{\partial \tilde{p}}{\partial x_i} + \frac{\partial}{\partial x_j}\left[\mu\left(\frac{\partial \tilde{u}_i}{\partial x_j} + \frac{\partial \tilde{u}_j}{\partial x_i}\right)\right] - \frac{\partial \tau_{ij}}{\partial x_j} \tag{2}$$

where, $\tilde{u}_i$ and $\tilde{p}$ are filtered mean velocity and filtered pressure, respectively. μ is dynamic viscosity, ρ is the density of fluid. $\tau_{ij} = \rho(\widetilde{u_i u_j} - \tilde{u}_i\tilde{u}_j)$ is SGS (subgrid-scale) stress resulting from the filtering operations, and is modeled by Eq. (3) as follows:

$$\tau_{ij} = -2\mu_t\tilde{S}_{ij} + \frac{1}{3}\tau_{ii}\delta_{ij} \tag{3}$$

In which, μ_t is subgrid-scale turbulent viscosity, and $\tilde{S}_{ij}$ is the rate-of–strain tensor for the resolved scale defined by Eq. (4):

$$\tilde{S}_{ij} = \frac{1}{2}\left(\frac{\partial \tilde{u}_i}{\partial x_j} + \frac{\partial \tilde{u}_j}{\partial x_i}\right) \tag{4}$$

Smagorinsky-Lilly model is used to calculate the subgrid-scale turbulent viscosity, μ_t defined as Eq. (5)

$$\mu_t = \rho L_S^2|\tilde{S}| = \rho L_S^2\sqrt{2\tilde{S}_{ij}\tilde{S}_{ij}} \tag{5}$$

where, L_S is the mixing length for subgrid-scales, defined as Eq. (6)

$$L_S = \min\left(\kappa\delta, C_s V^{1/3}\right) \tag{6}$$

In which, κ is the von Karman constant, 0.42, C_s is Smagorinsky constant is set as 0.032 following the suggestion in the reference (Oka and Ishihara, 2009), δ is the distance to the closest wall and V is the volume of a computational cell.

The volume of fluid (VOF) model is used in this study to model air and water. Volume fraction of water will be solved to capture the interface between air and water. Continuity equation for the volume fraction of water, α_w , reads:

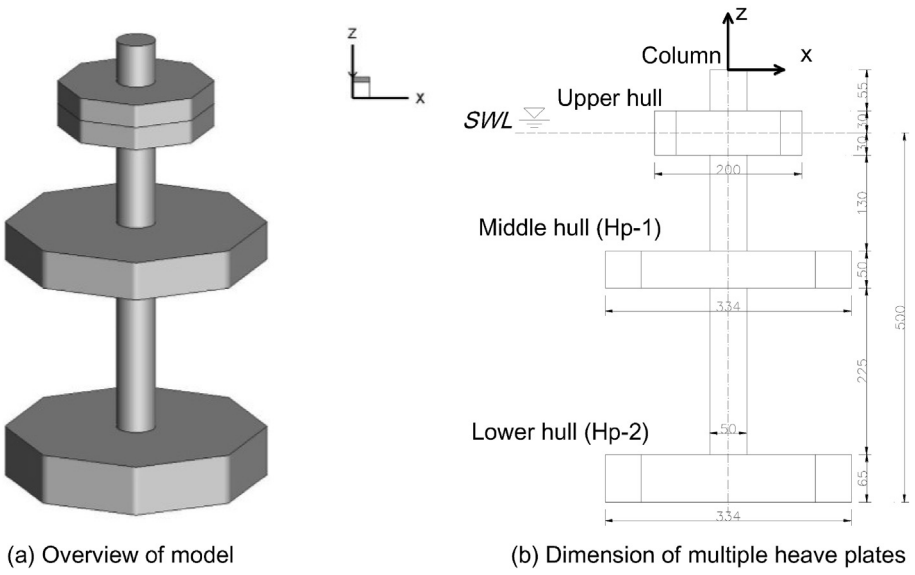

Fig. 1. Overview of the model and its dimension. Units (mm).

Table 1
Specifications of the scaled model geometry as shown in Fig. 1 (model scale 1:100).

Items	Symbol	Dimension (mm)
Model draft	h	500
Column diameter	D_c	50
Upper hull depth	h_p	30
Upper hull circumcircle diameter	D_p	200
Upper hull thickness	t_p	60
Middle hull (Hp-1) depth	$h_{Hp\text{-}1}$	210
Middle hull (Hp-1) circumcircle diameter	$D_{Hp\text{-}1}$	334
Middle hull (Hp-1) thickness	$t_{Hp\text{-}1}$	50
Lower hull (Hp-2) depth	$h_{Hp\text{-}2}$	500
Lower hull (Hp-2) circumcircle diameter	$D_{Hp\text{-}2}$	334
Lower hull (Hp-2) thickness	$t_{Hp\text{-}2}$	65

Note: Depth is measured from lower surface of the hull to the still water level.

$$\frac{1}{\rho_w}\left[\frac{\partial}{\partial t}(\alpha_w\rho_w) + \nabla(\alpha_w\rho_w\vec{v}_w)\right] = 0 \tag{7}$$

where, ρ_w is water density.

2.2. Computational domain and grid arrangement

Quality of grid plays a crucial role in the accuracy of numerical results. Grid independences are studied in section 2.7 to choose a reasonable grid system for following computations. The whole computational domain and grid around the model are displayed in Fig. 2. The computational domain is divided into two subdomains with respect to the simulated phases. The lower subdomain is used to simulate the phase of water and bottom of the subdomain is 3.1 h away from the still water level (SWL), where h is the draft of the model. The upper subdomain is utilized to consider the phase of air and top of the subdomain is 0.6 h above the SWL. In order to mitigate the reflecting flow from the boundary, side walls are located sufficiently far away from the model. The distance between the model and inlet and outlet is 40 D_c and 52 D_c, respectively, D_c is the diameter of the center column. The grid is refined at the locations where substantial flow separations are expected and near SWL to capture the shape of free surface as shown in Fig. 2 (b).

In this study, several configurations of multiple heave plates are simulated as described in section 2.4. The total cell number in the computational domain differs in the simulated models. The grid number ranges from 4.5 million to 4.9 million among those simulated models. Grid parameters near the model are described in Table 2.

2.3. Numerical schemes and boundary conditions

A finite volume method is employed for present time-dependent numerical simulations. A second order central difference scheme is used for the convective and viscous term. A first order implicit scheme is employed for the unsteady terms in the momentum equation as shown in Eq. (2), while an explicit approach is adopted for temporal discretization in the volume fraction equation as shown in Eq. (7). The courant number is 0.25, which means the time step for VOF simulation will be chosen to be one-fourth of the minimum transit time for any cell near the interface. A pressure-based segregated algorithm is used to solve the non-linear and coupled governing equations. A Pressure-Implicit with Splitting of Operators (PISO) algorithm is chosen to decrease the iterations for the pressure-velocity coupling solutions. Table 3 summarizes the numerical schemes used in this study. The governing equations are solved by a software ANSYS Fluent. The time step convergence and grid dependency are checked as mentioned by Oka and Ishihara (2009) and Stern et al. (2001).

Forced oscillation tests are carried out in the numerical simulations to evaluate the hydrodynamic coefficients, and dynamic mesh with layering mesh update method is utilized to simulate the movement of the model. The top of air phase and the bottom of water phase are treated as stationary boundaries while the model is oscillated up and down. Both split factor (a_s) and collapse factor (a_c) for the cells near the boundaries are 0.4 with respect to the first cell height (h_1) at moving boundaries. The layer of cells adjacent to the moving boundary is split or merged with layer of cells next to it based on the height of cells. The cell heights are allowed to increase until $h > (1 + a_s)h_1$, and the cell heights can be compressed until $h > a_c h_1$. The governing equations are solved based on newly determined cell coordinate.

Boundary conditions are summarized in Table 4. No-slip wall condition is adopted for the surface of model. Symmetry conditions is utilized for both the top of air phase, the bottom of water phase and the side wells, which indicates the shear stress at the boundary is zero. Outflow boundary condition (zero gradient of velocity) is applied to the inlet and outlet as the water tank test. In the LES model, the wall shear stress is obtained from the laminar stress-strain relationship when the centroid of wall adjacent cell is in the laminar sublayer with the height of $y+ = 11.25$ as shown in Fluent Theory Guide (Fluent Theory Guide, 2012). If the

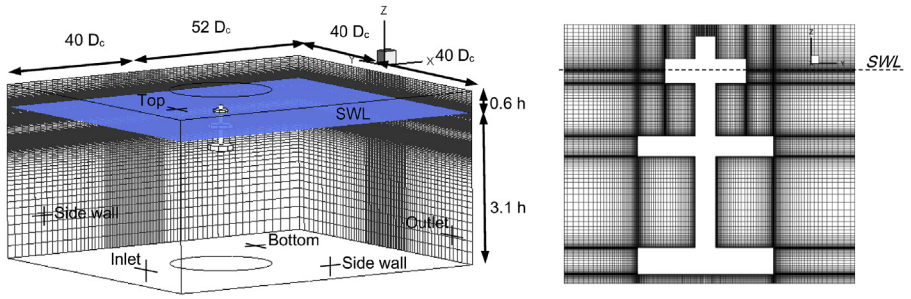

(a) Computational domain (b) Grid around the model

Fig. 2. Computational domain and grid around the model.

Table 2
Description of grid parameters near the model.

Parameters	Value
First layer in the radial direction (mm)	0.257
First layer in the vertical direction (mm)	0.6
Expanding factor	1.0–1.2
Grid number (million)	4.5–4.9

Table 3
Summary of numerical schemes.

Items	Scheme
Turbulence model	Smagorinsky-Lilly (C_s = 0.032)
Spatial discretization method	Second order central difference scheme
Time discretization method for momentum equation	First order implicit scheme
Time discretization method for volume fraction equation	Explicit scheme
Pressure-velocity coupling	Pressure-Implicit with Splitting of Operators (PISO)
Courant number	0.25
Dynamic mesh	Layering

mesh is too coarse to resolve the laminar sublayer, it is assumed that the centroid of the wall adjacent cell falls within the logarithmic region of the boundary layer, and the law-of-the-wall is employed.

2.4. Simulation cases

The model shown in Fig. 1 is firstly studied by vertically forced oscillation test. The model is vertically forced to oscillate sinusoidally as in Eq. (8).

$$x(t) = a\ \sin(\omega t) \tag{8}$$

where, $x(t)$ is the time-varying displacement in the vertical direction in this study, a is the oscillating amplitude, ω is the oscillating angular frequency ($= 2\pi/T$), and T is the oscillating period.

In the numerical simulations for the model shown in Fig. 1, the oscillating amplitude is 0.02 m, and oscillating periods vary from 0.8 s to 2.1 s. The tested cases for the multiple heave plates are listed in Table 5. The KC number and frequency number, β, shown in Table 5 are defined as follows:

$$KC = \frac{V_{max}}{D_{Hp}f} = \frac{\omega a}{D_{Hp}f} = \frac{2\pi a}{D_{Hp}} \tag{9}$$

$$\beta = \frac{Re}{KC} = \frac{V_{max}D_{Hp}/\nu}{V_{max}/D_{Hp}f} = \frac{D_{Hp}^2 f}{\nu} \tag{10}$$

where, V_{max} is the maximum oscillating velocity, a is the oscillating amplitude, D_{Hp} is the circumcircle diameter of the heave plate, f is the oscillating frequency and ν is the kinematic viscosity of water.

In this study, the effect of spacing between Hp-1 and Hp-2 (see Fig. 1) on hydrodynamic coefficients is also investigated. Moreover, influences of the diameter ratio (D_{Hp}/D_c) and the aspect ratio (t_{Hp}/D_{Hp}) on the hydrodynamic coefficients are studied as well. Several configurations of the model are simulated in terms of different spacing, diameter ratios and aspect ratios as specified in Table 6, Table 7 and Table 8, respectively. The spacing between Hp-1 and Hp-2 changes from 0.020 m to 0.225 m, while the spacing between upper hull and Hp-1 remain unchanged as shown in Table 6. As a result, the model draft varies from 0.295 m to 0.5 m. The diameter and thickness of heave plates are kept as a constant. Consequently, the spacing ratio of heave plates in present numerical simulations ranges from 0.060 to 0.674. In Table 7, the thickness and circumcircle diameters of octagonal Hp-1 and Hp-2 remain unchanged, while the diameter of column changes from 0.042 m to 0.167 m. Therefore, the diameter ratio of heave plates ranges from 2.0 to 8.0. Only a single heave plate is used to study the effect of aspect ratio on hydrodynamic coefficients. In Table 8, the thickness of the heave plate changes from 0.00334 m to 0.0668 m, corresponding to the aspect ratio ranging from 0.010 to 0.200. The oscillating parameters used in this study are specified in Table 9.

2.5. Definition of hydrodynamic coefficients

The time series of predicted hydrodynamic force, $F_H(t)$, is obtained by subtracting the buoyancy force, F_b, and hydrostatic force, $F_K(t)$, from the total predicted force, $F(t)$, which is obtained from the surface pressure and shear on the model.

$$F_H(t) = F(t) - F_b - F_K(t) \tag{11}$$

where,

$$F_b = \rho_w g \forall \tag{12}$$

$$F_K(t) = -K_R\ x(t) \tag{13}$$

ρ_w is the water density, g is the gravitational acceleration, $\forall$ is the displaced volume by the model at its mean position, K_R is the hydrostatic stiffness and $K_R = \rho_w g A_w$, A_w is the water plane area, and $x(t)$ is the time-varying displacement of the model.

The hydrodynamic force, $F_H(t)$, can be expressed in the form of Morison's equation as follows:

$$\begin{aligned} F_H(t) &= -C_a M_{at}\,\ddot{x}(t) - 0.5 C_d \rho_w A |\dot{x}(t)|\dot{x}(t) \\ &= \frac{1}{3} C_a \rho_w D_{Hp\text{-}1}^3 a\omega^2 \sin(\omega t) \\ &\quad -\frac{1}{2} C_d \rho_w A\ (a\omega)^2 |\cos(\omega t)|\cos(\omega t) \end{aligned} \tag{14}$$

Table 4
Summary of boundary conditions.

Items	Boundary conditions
Model walls	No-slip wall
Top of air phase	Symmetry
Bottom of water phase	Symmetry
Side walls	Symmetry
Inlet and Outlet	Outflow (zero gradient of velocity)

Table 5
List of cases in the forced oscillation test.

Period (s)	Amp. (m)	KC	β
0.8	0.02	0.38	139028
1.1	0.02	0.38	101111
1.3	0.02	0.38	85556
1.7	0.02	0.38	65425
2.1	0.02	0.38	52963

where C_a is the added mass coefficient, C_d is the drag coefficient, $M_{at}= (1/3\rho_w D^3_{Hp\text{-}1})$ is the theoretical added mass of the heave plate as defined in reference (Sarpkaya, 2010), $D_{Hp\text{-}1}$ is the circumcircle diameter of the heave plate Hp-1, and $A = (1/4\pi D^2_{Hp\text{-}1})$ is the characteristic area of the heave plate, $\dot{X}(t)$ and $\ddot{X}(t)$ are the velocity and acceleration of the model motion, respectively.

As shown in the reference (Sarpkaya, 2010), Fourier averages of C_a and C_d are obtained as follows:

$$C_a = \frac{\int_0^T F_H(t)\sin(\omega t)dt}{\frac{1}{3}\rho_w D^3_{Hp\text{-}1}a\omega^2\int_0^T \sin^2(\omega t)dt} = \frac{3}{\pi\omega a\rho_w D^3_{Hp\text{-}1}}\int_0^T F_H(t)\sin(\omega t)dt \quad (15)$$

$$C_d = -\frac{\int_0^T F_H(t)\cos(\omega t)dt}{\frac{1}{2}\rho_w A(\omega a)^2\int_0^T |\cos(\omega t)|\cos(\omega t)\cos^2(\omega t)dt} = -\frac{3}{4\rho_w A\omega a^2}\int_0^T F_H(t)\cos(\omega t)dt \quad (16)$$

The Parameters of the model are described in Table 10.

2.6. Water tank test

A water tank test was carried out in this study to validate the predicted C_a and C_d by the numerical simulations. Dimensions of the water tank are 100 m length, 5 m width, and 2.65 m depth. The water depth set up in this experiment is 2.0 m. Overview of the tested model is shown in Fig. 3. The detailed dimensions of the multiple heave plates are described in Table 1. The cases conducted in the water tank test are listed in Table 5.

The time series of measured hydrodynamic force, $F_H(t)$, is obtained by subtracting the buoyancy force, F_b, inertia force, $F_I(t)$, and hydrostatic force, $F_K(t)$, from the measured total force, $F(t)$.

$$F_H(t) = F(t)\text{-}F_b\text{-}F_I(t)\text{-}F_K(t) \quad (17)$$

where,

$$F_I(t) = \text{-}M\,\ddot{X}(t) \quad (18)$$

M is the model mass including the mass of attachment used to connect the force balance and the model, $\ddot{X}(t)$ is the acceleration of the model motion, F_b and $F_K(t)$ are evaluated by Eq. (12) and Eq. (13), respectively.

The parameters of the model are listed in Table 10. When the hydrodynamic force is obtained according to Eq. (17), the C_a and C_d are identified by Eqs. (15) and (16), respectively. In order to mitigate the unstable result owing to measurement uncertainties, ten periods of measured data are used in the data analysis.

2.7. Validation of numerical results

In this section, time history of predicted and measured hydrodynamic forces is presented in a non-dimensional form as follows:

$$C_F(t^*) = \frac{F_H(t)}{\frac{1}{2}\rho_w A(\omega a)^2}; t^* = \frac{t}{T} \quad (19)$$

where, $F_H(t)$ is the predicted or measured hydrodynamic forces according to Eq. (11) and Eq. (17), A is the characteristic area of the heave plate, and t^* is the non-dimensional time.

The predicted and measured time history of non-dimensional hydrodynamic force is illustrated in Fig. 4. The inertia contribution from force balance was excluded when analyzing the experimental data and the experimental data is filtered with cut-off frequency to remove noise in signal. Eight-period data from time zero was removed from experimental data to reach stable time series of hydrodynamic force. Consequently, the predicted hydrodynamic force matches well with the measurement in terms of phase and the error of predicted amplitude is −1.3%. Time series of the predicted hydrodynamic force becomes stable after the initial first period. In order to prevent the effect from the initial unstable solution on the accuracy of hydrodynamic coefficients, the simulated data from the third period to the fifth period are chosen in the data analysis, and the averaged coefficients are used in this paper.

The predicted and measured C_a and C_d in the case of an oscillating period of 1.3 s are presented in Fig. 5 for the purpose of grid and time step independence study. It is found from Fig. 5(a) that coarse grid brings about overestimation of hydrodynamic coefficients, especially in the prediction of C_d, which implies that the fine grids around the corners of the heave plates are required to accurately simulate the flow separation. The results obtained from the finest grid match well with those obtained from the experiment. Numerical results show a weak dependence on the time step as shown in Fig. 5(b). It should be noted that the large time step

Table 6
Specifications of the configurations in different spacing ratios (The values only shown in Case1 are used for all cases).

Items		Case 1	Case 2	Case 3	Case 4	Case 5	Case 6
Columns diameter (mm)	D_c	0.050					
Upper hull circumcircle diameter (mm)	D_p	0.200					
Hp-1 (Hp-2) circumcircle diameter (mm)	$D_{Hp\text{-}1}$, $D_{Hp\text{-}2}$	0.334					
Diameter ratio	$D_{Hp\text{-}1}/D_c$	6.680					
Hp-1 aspect ratio	$t_{Hp\text{-}1}/D_{Hp\text{-}1}$	0.150					
Hp-2 aspect ratio	$t_{Hp\text{-}2}/D_{Hp\text{-}2}$	0.195					
Spacing between Hp-1 and Hp-2 (mm)	L	0.020	0.040	0.075	0.125	0.175	0.225
Model draft	h	0.295	0.315	0.350	0.400	0.450	0.500
Spacing ratio	$L/D_{Hp\text{-}1}$	0.060	0.120	0.224	0.374	0.524	0.674

Table 7
Specifications of the configurations in different diameter ratios (The values only shown in Case 1 are used for all cases).

Items		Case 1	Case 2	Case 3	Case 4	Case 5	Case 6	Case 7
Columns diameter (m)	D_c	0.167	0.095	0.084	0.067	0.056	0.050	0.042
Upper hull circumcircle diameter(m)	D_p	0.200						
Hp-1 (Hp-2) circumcircle diameter(m)	$D_{Hp\text{-}1}$, $D_{Hp\text{-}2}$	0.334						
Hp-1 aspect ratio	$t_{Hp\text{-}1}/D_{Hp\text{-}1}$	0.150						
Hp-2 aspect ratio	$t_{Hp\text{-}2}/D_{Hp\text{-}2}$	0.195						
Diameter ratio	$D_{Hp\text{-}1}/D_c$	2.0	3.5	4.0	5.0	5.96	6.68	8.0
Spacing between Hp-1 and Hp-2 (m)	L	0.225						
Spacing ratio	$L/D_{Hp\text{-}1}$	0.674						

Table 8
Specifications of the configurations in different aspect ratios (The values only shown in Case1 are used for all cases).

Items		Case 1	Case 2	Case 3	Case 4	Case 5
Columns diameter (m)	D_c	0.050				
Hp-2 circumcircle diameter(m)	$D_{Hp\text{-}2}$	0.334				
Hp-2 thickness (m)	$t_{Hp\text{-}2}$	0.00334	0.01002	0.0167	0.0334	0.0668
Aspect ratio	$t_{Hp\text{-}2}/D_{Hp\text{-}2}$	0.010	0.030	0.050	0.100	0.200

Table 9
Description of the oscillation parameters used in the numerical simulations.

Items	Symbol	Value
Oscillating amplitude (m)	a	0.02
Oscillating period (s)	T	0.8
KC number	KC	0.38
Frequency parameter	β	139028

Table 10
Description of parameters of the model as shown in Fig. 1.

Parameters	Symbol	Value
Characteristic area (m^2)	A	0.0789
Displaced volume (m^3)	∀	0.01062
Water density (kg/m^3)	ρ_w	1000
Hydrostatic stiffness (N/m)	K_R	277.4

will cause large courant number, which significantly impacts the convergence of numerical iterations. Therefore, a sufficiently small time step is required in VOF method to simulate the unsteady flow. Consequently, the finest grid and a time step of 0.001 s are used in following numerical simulations.

Fig. 6 shows predicted and measured C_a and C_d for different oscillating periods. C_a exhibits negligible oscillating periods dependence. It is also found that C_a is less than 2.0 even though one additional surface piercing plate is expected to provide some added mass. The reason is primarily due to the fact that the shape of present heave plates is octagonal cross-section, which provides smaller added mass compared with the circular plate along with the presence of center columns depriving contribution to added mass approaching theoretical value. Predicted and measured C_d are also found almost independent of oscillating period as shown in Fig. 6(b).

As a conclusion from this section, predicted hydrodynamic coefficients for the multiple heave plates shows favorable agreement with those obtained from the water tank test, and the C_a is almost independent of frequency parameter, β, while C_d shows weak dependence on frequency parameter, β.

3. Mechanism of hydrodynamic force and effect of geometric parameters

In this section, mechanism of hydrodynamic force on the multiple heave plates are clarified, and the effects of geometrical parameters, such

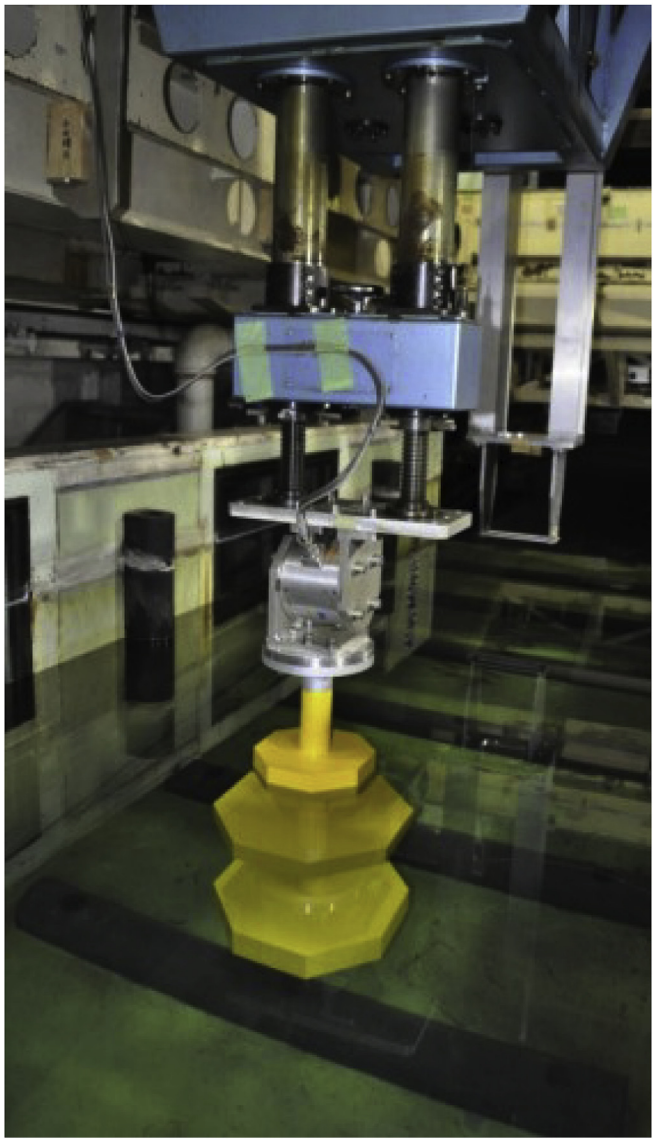

Fig. 3. Overview of the tested model in the water tank test.

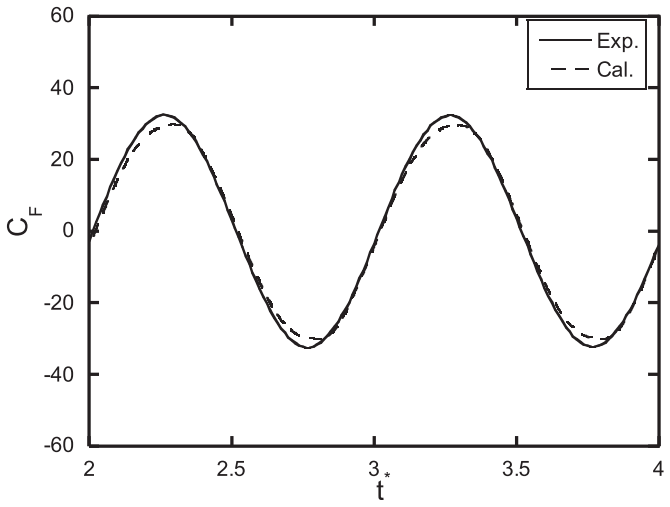

Fig. 4. Comparison of the predicted and measured hydrodynamic force coefficient.

as spacing ratio, diameter ratio and aspect ratio on hydrodynamic coefficients are then discussed. The numerical results are also used in Section 4 to provide database for deriving formulas of hydrodynamic coefficients. The proposed formulas can be used in design of offshore structures with heave plates.

3.1. Mechanism of hydrodynamic force

According to the predicted hydrodynamic force on each heave plate, i.e. Hp-1 and Hp-2 as shown in Fig. 1, the C_a and C_d of each heave plate are evaluated by Eq. (15) and Eq. (16), respectively. The hydrodynamic force used to evaluate the C_a and C_d of each plate, $F_{H,Hp\text{-}i}(t)$, are obtained by following expression:

$$F_{H,Hp\text{-}i}(t) = \rho_w g h_{t,Hp\text{-}i} A_{t,Hp\text{-}i} - \rho_w g h_{b,Hp\text{-}i} A_{b,Hp\text{-}i} + \rho_w g (A_{b,Hp\text{-}i} - A_{t,Hp\text{-}i}) x(t) + F_{Hp\text{-}i}(t) \quad (20)$$

where, $F_{Hp\text{-}i}(t)$ refers to the calculated total force which includes the effect of hydrostatic pressure, $h_{b,Hp\text{-}i}$ and $h_{t,Hp\text{-}i}$ represent the depth of lower and upper surface of the heave plate Hp-i from the still water level, respectively; $A_{b,Hp\text{-}i}$ and $A_{t,Hp\text{-}i}$ are the characteristic area of lower and upper surface of heave plate Hp-i, respectively; $x(t)$ is the time-varying displacement as given in Eq. (8).

Fig. 7 shows the predicted C_a and C_d of Hp-1 and Hp-2 varying with oscillating periods. It is found from Fig. 7 (a) that C_a of Hp-2 is slightly larger than that Hp-1, which is because mass of an ellipsoid of water enclosing the Hp-2 is larger than that of Hp-1 due to absence of center column below Hp-2. C_d of Hp-1 is larger than that of Hp-2, especially in low oscillating periods as shown in Fig. 7 (b), which is because that the thinner plate, the larger C_d. The significant nonlinearity of oscillating flow in higher oscillating frequency makes the differences between Hp-1 and Hp-2 more remarkable. One additional simulation is carried out to investigate the effect of upper hull on the hydrodynamic coefficient of Hp-1. As seen from Fig. 7, Ca of Hp-1 is close to Ca of Hp-2 when upper hull is absent.

The dynamic pressure will be used to explain the force acting on each heave plate, and is made a non-dimensional form as follows:

$$C_p = \frac{p\text{-}\rho_w g h}{1/2\rho_w(\omega a)^2} \quad (21)$$

where, p is the pressure in the flow field, which contains hydrodynamic pressure and hydrostatic pressure, h is the depth of the computational cell from the still water level.

The time history of non-dimensional hydrodynamic force on each heave plate is shown in Fig. 8. Fig. 9(b) shows the corresponding instantaneous dynamic pressure distribution around the multiple heave plates in one oscillating period. At time $t = 0$, due to the previous accelerating ascent, the upper surface of Hp-1 acts as the like stagnation, and is experiencing a positive dynamic pressure at this moment. In addition, the dynamic pressure around the lower surface of Hp-1 is almost zero at this moment. Therefore, the resultant hydrodynamic force acting on Hp-1 is negative as shown in Fig. 8. From this moment, the model starts to decelerate. The upward moving flow caused by previous ascending model keeps moving upward at time 0, and velocity of the moving model is smaller than that of moving flow around it. Then, the upper surface of Hp-1 starts to locate in the wake of moving flow. As a result, the upper surface of Hp-1 is subjected to negative dynamic pressure while the lower surface is experiencing positive dynamic pressure at time $t = 2/8$ T. The substantial magnitude of dynamic pressure at this moment leads to the maximal positive hydrodynamic force within the oscillating period (see Fig. 8). The coming distribution of dynamic pressure at time $t = 4/8$ T and $t = 6/8$ T are very similar to those at $t = 0$ and $T = 2/8$ T, whereas the sign of dynamic pressure is reverse. Similar phenomena and conclusions can also be found for the Hp-2. The dynamic pressures around Hp-1 and Hp-2 at time $t = 2/8$ T are almost same, but the central column does not pierce the plate Hp-2, being absent from the lower surface. As a result, the maximum hydrodynamic force on Hp-2 is slightly larger than that of Hp-1 as shown in Fig. 8, which leads to a larger C_a for Hp-2 as shown in Fig. 7(a).

3.2. Effect of spacing ratio and diameter ratio

The cases listed in Tables 6 and 7 are conducted to systematically study the effect of spacing ratio ($r_L = L/D_{Hp1}$) and diameter ratio ($R_d = D_{Hp\text{-}1}/D_c$), respectively. Fig. 9(a) and (b) show the dynamic pressure distribution for two representative spacing ratios, i.e. $r_L = 0.06$ and $r_L = 0.674$. The variation of C_a and C_d with different spacing ratios is

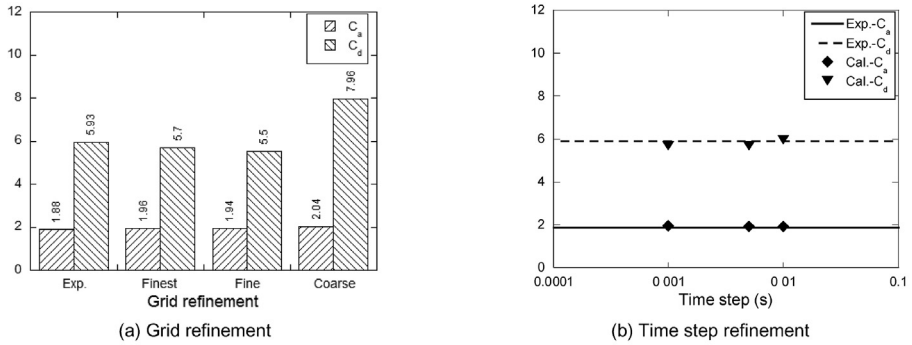

Fig. 5. Effect of grid and time step refinements on the accuracy of predicted hydrodynamic coefficients.

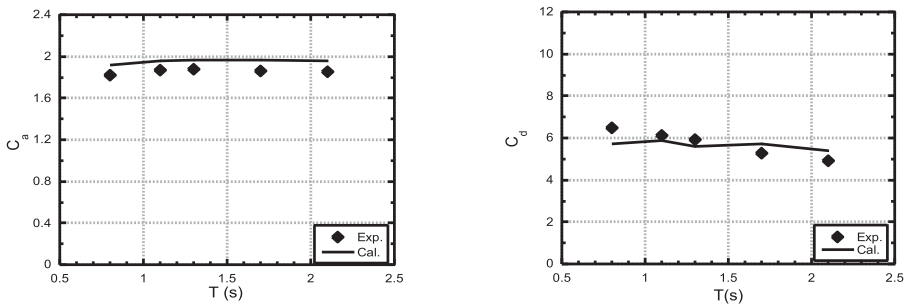

Fig. 6. Comparison of predicted and measured added mass and drag coefficients for various oscillating periods.

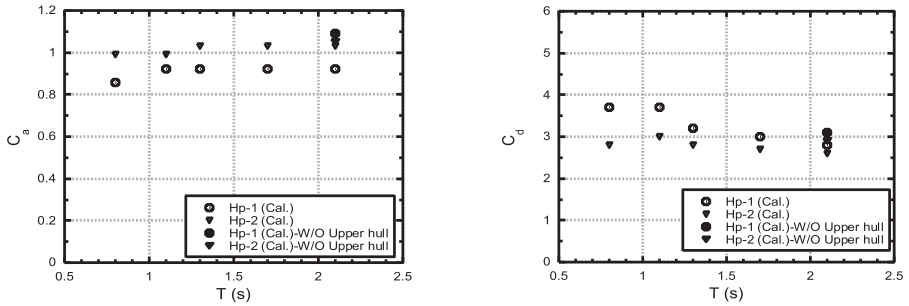

Fig. 7. Predicted added mass and drag coefficients for Hp-1 and Hp-2 for various oscillating periods.

shown in Fig. 18 in section 4.2. C_a increases as the spacing between Hp-1 and Hp-2 increases. In the case of $r_L = 0.674$, the sign of dynamic pressure on upper and lower surface of heave plate Hp-2 are opposite at time t = 2/8 T as shown in Fig. 9(b), while the sign of dynamic pressure is identical in the case of $r_L = 0.06$ as shown in Fig. 9(a). As a result, the hydrodynamic force on the heave plate is smaller in the case of $r_L = 0.06$, and leads to the smaller added mass as indicated in Fig. 18(a). It is also found from Fig. 18(a) that the slope of variation of C_a decreases as the spacing ratios increase, which indicates that interaction between Hp-1 and Hp-2 becomes weak in larger spacing ratios. It is expected that the C_a will no longer increase when the spacing ratio exceeds a critical value. Similarly, C_d shown in Fig. 18(b) also increases as the spacing ratio increases. Fig. 10(a) and (b) show the instantaneous flow vortex shedding pattern for the two representative spacing ratios, i.e. $r_L = 0.06$ and $r_L = 0.674$. The non-dimensional vorticity shown in Fig. 10 is defined as follows:

$$W_x^* = W_x \cdot \frac{D_{Hp\text{-}1}}{V_{max}} \tag{22}$$

where, W_x is X-vorticity, V_{max} is the maximum oscillating velocity ($= \omega a$).

The reason why C_d is smaller in case of smaller spacing ratio is because vortex shedding around Hp-1 and Hp-2 are interactive over the whole oscillating period as shown in Fig. 10(a), which significantly reduces the drag force. When the spacing ratio exceeds a critical value, the vortex shedding around Hp-1 and Hp-2 becomes independent as shown in Fig. 10(b), and the C_d reaches its maximum.

The variation of C_a and C_d with different diameter ratios is shown in Fig. 19 in section 4.2. Fig. 9(b) and (c) exhibits dynamic pressure distribution for two representative diameter ratios, i.e. $R_d = 6.68$ and $R_d = 2$. Fig. 10(b) and (c) show the corresponding instantaneous flow vortex shedding pattern in one oscillating period. It is seen from Fig. 19(a) that C_a increases as the diameter ratio increases. Even though the dynamic pressure distributions as shown in Fig. 9(b) and (c) are almost same between those two representative diameter ratios, the wet surface of the plate with smaller diameter ratio is smaller than that with larger diameter ratio as shown in Fig. 9(c), which causes smaller hydrodynamic force, and results in smaller C_a as shown in Fig. 19(a). Similarly with the case of spacing ratio, the slope of variation of C_a decreases as the diameter ratio increases, which is because the increase rate of wet surface decreases as the diameter ratio increases. In contrast to C_a, C_d is found to be independent of the diameter ratios as shown in Fig. 19(b) within the range of diameter ratio from 2.0 to 8.0. It should be noted that the drag force mainly comes from the vortex shedding around the sharp edges of heave plates. As seen from Fig. 10(b) and (c), the vortex shedding near the sharp edges is not affected when the diameter ratio decreases. Therefore, C_d keeps almost unchanged. By further increasing the diameter of the column, the side wall of the column might disturb the vortex

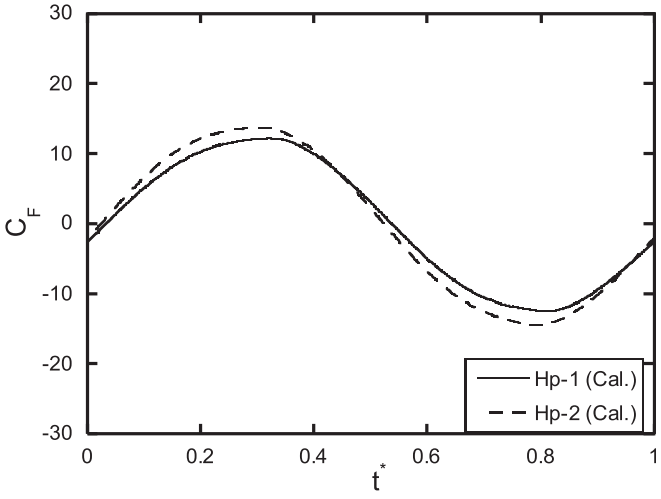

Fig. 8. Time series of predicted non-dimensional hydrodynamic force acting on each plate.

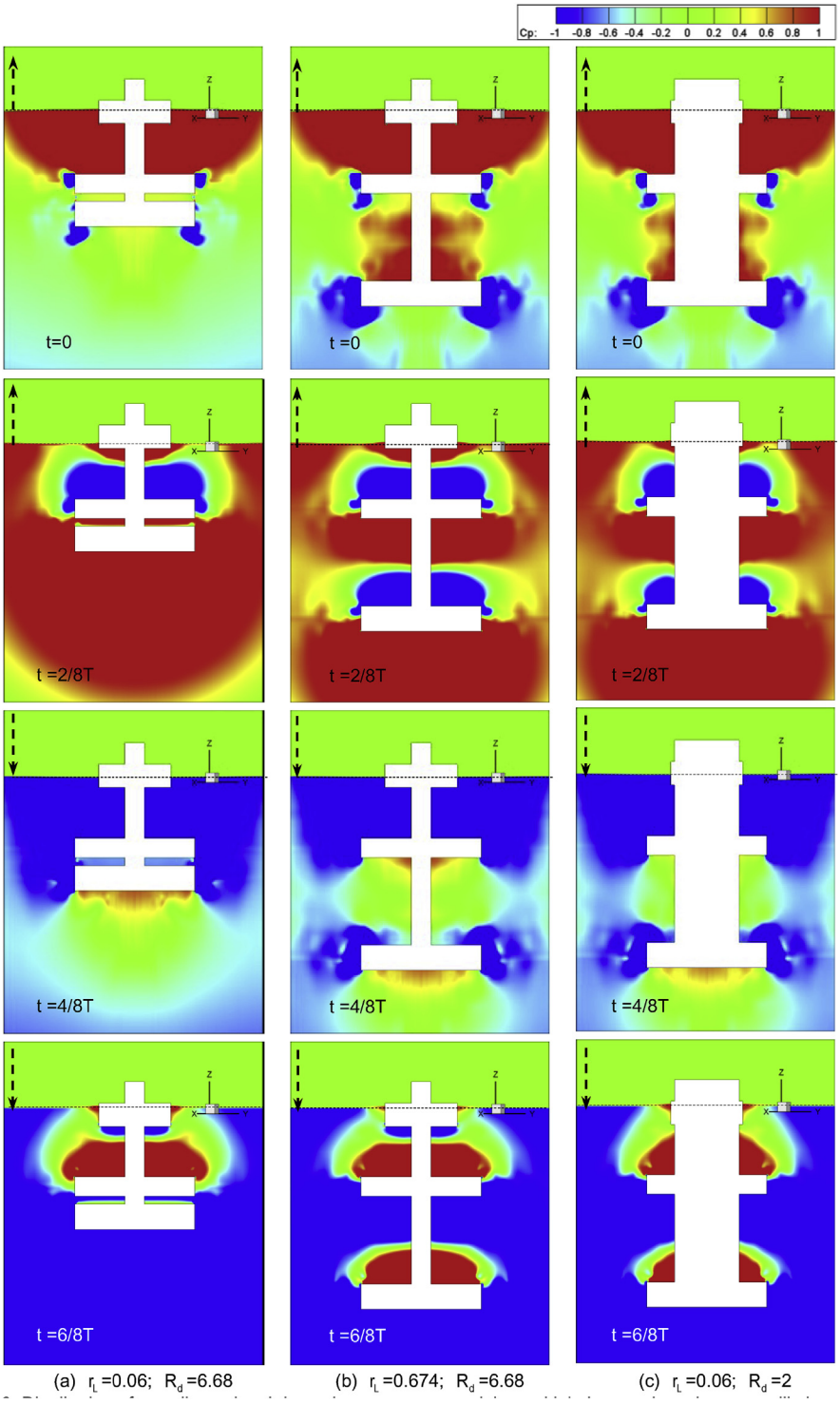

Fig. 9. Distribution of non-dimensional dynamic pressure around the multiple heave plates in one oscillating period.

shedding around the heave plate, probably resulting in smaller C_d. However, such smaller diameter ratio is rarely used in the application of heave plate.

According to Figs. 18(b) and 19(b), C_d provided by the double heave plates is less than 7.0, which is even smaller than that of a single heave plate predicted or measured in the literature (Lopez-Pavon and Souto-Iglesias, 2015; Li et al., 2013). The reason is primarily owing to the fact that the aspect ratio of the heave plates used in this study is significantly larger than those in the references.

3.3. Effect of aspect ratio

The cases listed in Table 8 are conducted to systematically study the effect of aspect ratio ($r_t = t_{Hp}/D_{Hp}$) on hydrodynamic coefficients. The thickness of the octagonal single heave plate is varied from 3.34 mm to 66.8 mm, corresponding to the aspect ratio ranging from 0.01 to 0.2. The draft of the heave plate is identical to the depth of Hp-2 shown in Fig. 1. The numerically identified C_a and C_d varying with the aspect ratios are shown in Fig. 12 in section 4.1. It is found that C_a is independent of the aspect ratio because the change of the thickness has no influence on the

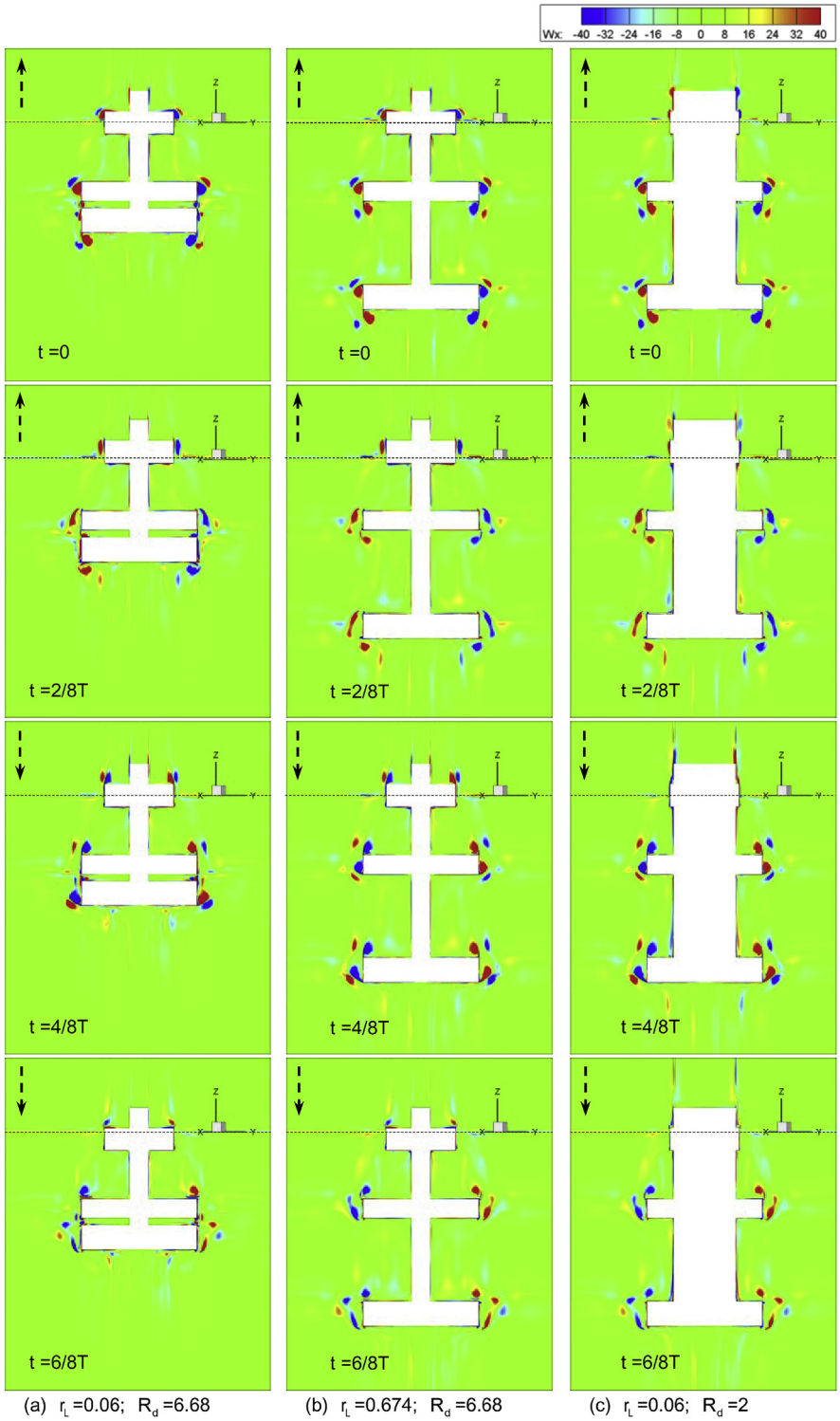

Fig. 10. Instantaneous flow vortex shedding pattern around the multiple heave plates in one oscillating period.

change in characteristic area of upper and lower surface of the heave plate, and has no remarkable impact on the dynamic pressure distribution. In contrast to the C_a, C_d is strongly dependent of the aspect ratio as shown in Fig. 12(b). It is found that C_d decreases as the aspect ratio increases. Variations of the thickness generate distinct vortex shedding patterns, which have been reported in the references (Tao and Thiagarajan, 2003a, 2003b). Fig. 11 shows the instantaneous vortex shedding around the heave plate with two representative aspect ratios at time $t = 0$ when the heave plate is moving upward from its mean position. The unidirectional vortex shedding happens in the case of small aspect ratio as shown in Fig. 11(a), while the interactive vortex shedding is observed under the condition of large aspect ratio in Fig. 11(b). It is the emerging interaction of vortex shedding from the upper and lower surface of heave plate that leads to the decreased C_d. As the aspect ratio further increases, independent vortex shedding pattern will happen as studied by Tao and Thiagarajan (2003a).

The aspect ratio of the Hp-1 and Hp-2 shown in Fig. 1 is 0.15 and 0.20, respectively. Therefore, C_d is expected smaller than those predicted

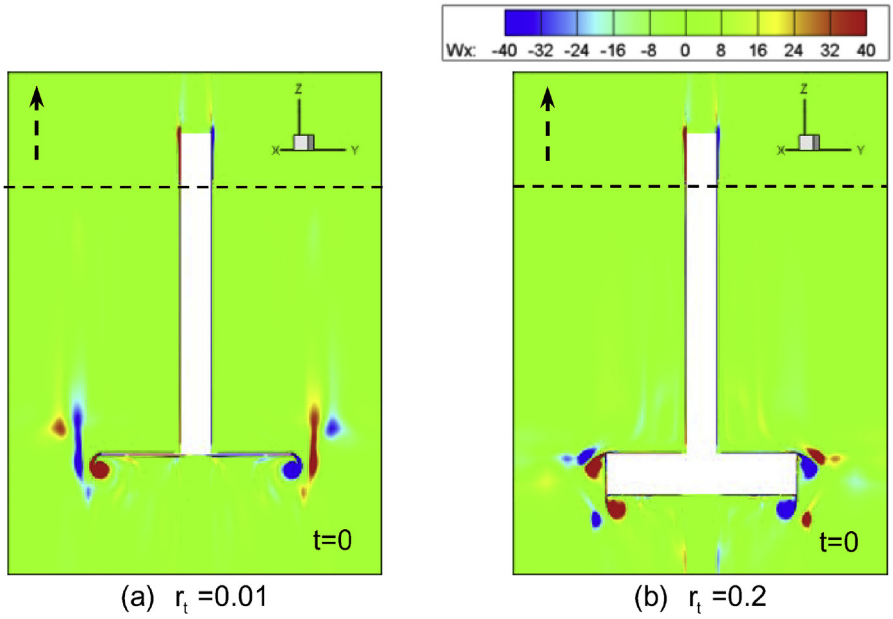

Fig. 11. Instantaneous flow vortex pattern around the single heave plate with two different aspect ratios at oscillating time t = 0.

and measured in the literature (Lopez-Pavon and Souto-Iglesias, 2015; Li et al., 2013, WindFloat), where the aspect ratio is around 0.005–0.01. In general, the heave plate mainly has two functions. One is used to reduce the heave motion. In this sense, the heave plate should be designed as thin as possible to reach sufficiently large C_d, such as the application in WindFloat (WindFloat). The other is used to stabilize the structure by lowering the center of gravity. In this respect, the heave plate would be designed with a certain thickness to allow for pouring the ballast water. The present multiple heave plates aim to achieve the mentioned two functions at same time. The usage of double heave plates makes C_d reaches almost 7.0, which significantly increases the damping in the heave direction.

As a conclusion from this section, change of aspect ratio only influences the C_d. Change of the spacing ratio between multiple heave plates affects both C_a and C_d, while the variation of diameter ratio only affects C_a. Formulas of C_a and C_d according to those sensitive geometrical parameters will be established in next section.

4. Formulas of hydrodynamic coefficients

In this section, the formula of C_a and C_d are proposed considering various geometric parameters and KC number. First, the formulas for a single heave plate with various cross-sections are improved and validated against published data in the literature and present numerical simulations. Then, the formulas for each plate in the double heave plates considering the spacing and diameter ratio are proposed and validated by the numerical simulations.

4.1. Added mass and drag coefficient for a single heave plate

Theoretical added mass of a heave plate without an attached column equals to the mass of an ellipsoid of water enclosing the heave plate (Sarpkaya, 2010). The ellipsoid is separated into two half ellipsoids by a finite distance (thickness of the heave plate). When one column is applied on the top of heave plate, the volume taken by the column is excluded to represent the effective added mass. Consequently, formula of C_a for a single circular heave plate with a column is firstly proposed by Tao et al. (2007) and rewritten as follows:

$$C_a = 1 - \frac{1}{4}\left[3r_d^2\sqrt{1-r_d^2} + \left(1-\sqrt{1-r_d^2}\right)^2\left(2+\sqrt{1-r_d^2}\right)\right] \quad (23)$$

where, $r_d = D_c/D_{Hp}$, which is the reciprocal of diameter ratio R_d.

The proposed formula by Tao et al. (2007) is suitable for the case with very low KC number. As mentioned in the references (Lopez-Pavon and Souto-Iglesias, 2015; Tao et al., 2004, 2007; Tao and Cai, 2004) that C_a increases as KC number increases. Therefore, a correction factor, k_1 , associated with KC number should be considered in the formula. In addition, it is found from the literature (Li et al., 2013; Tao et al., 2004; Tao and Dray, 2008) that C_a is strongly dependent on heave plate

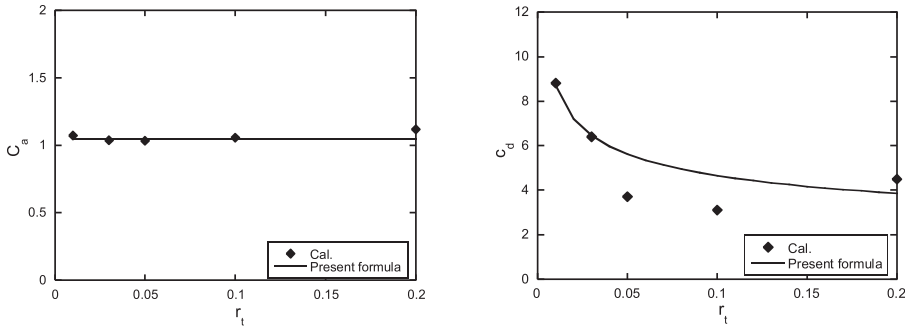

(a) Added mass coefficient (b) Drag coefficient

Fig. 12. Comparison of numerical identified and formula predicted added mass and drag coefficients for the single octagonal heave plate with different aspect ratios.

cross-sections, such as circular and rectangular heave plate. Thus, a shape correction factor, k_2 , which represents the change of cross-section is needed when applying the formula for the heave plate other than circular ones. In this study, an integrated correction factor, k , expressed by the multiplication of k_1 and k_2 is used to take into account the effect of both KC number and shape correction factor. The correction factor, k , is used to modify the diameter of the ellipsoid representing the added mass. A linear function of KC number is adopted for k_1 in this study. In the shape correction factor, k_2 , there is no reduction for the diameter of circular heave plate, while the equivalent diameter is reduced to its 95% for an octagonal heave plate, and is reduced to its 75% for a square heave plate. They are purely empirical values based on the fitting of Ca for an octagonal heave plate and a square heave plate. It should be noted that the diameter is reduced with respect to the circumcircle diameter of the cross-section. As a result, formula of C_a for a single heave plate attached with a column is improved as follows:

$$C_a = k^3 - \frac{1}{4}\left[3r_d^2\sqrt{k^2 - r_d^2} + \left(k - \sqrt{k^2 - r_d^2}\right)^2\left(2k + \sqrt{k^2 - r_d^2}\right)\right] \tag{24}$$

$$k = k_1 \cdot k_2 \tag{25}$$

$$k_1 = 1 + 0.2\ KC \tag{26}$$

$$k_2 = \begin{cases} 1.00; & \text{Circular heave plate} \\ 0.95; & \text{Octagonal heave plate} \\ 0.75; & \text{Square heave plate} \end{cases} \tag{27}$$

where, $r_d = D_c/D_{Hp}$, which is the reciprocal of diameter ratio R_d, k represents the correction factor which is a function of KC number and heave plate cross-section, and KC refers to the KC number.

As mentioned in section 3.3 and previous studies, C_d is dependent of aspect ratio, r_t, and KC number. According to the proposed formula ($C_d = A(KC)^n$) by Graham (1980), Tao and Thiagarajan (2003a) identified the coefficients (A and n) for three typical vortex shedding regimes. Whereas, C_d actually varies with the aspect ratio, r_t, even in one specific defined vortex shedding regime. In other words, the coefficient A in the formula should be a function of aspect ratio rather than a constant. In this study, by fixing the KC number as unit one, the coefficient A as a function of aspect ratio, r_t, is evaluated based on the data of C_d versus aspect ratio, r_t, in the study by Tao and Thiagarajan (2003a). Then, the coefficient n is evaluated. The evaluation of coefficient n for square heave plate follows the abovementioned procedure according to the data in the study by Li et al. (2013). In this study, a new formula of C_d is proposed to represent the effect of both aspect ratio and KC number for a single heave plate and is improved as below:

$$C_d = \min\left\{1.7r_t^{-1/3.7}(KC)^{-1/k_3}, 12\right\} \tag{28}$$

$$k_3 = \begin{cases} 2.5; & \text{Circular heave plate} \\ 2.5; & \text{Octagonal heave plate} \\ 3.0; & \text{Square heave plate} \end{cases} \tag{29}$$

where, $r_t (= t_{Hp}/D_{Hp})$ is the aspect ratio of heave plate, t_{Hp} is the thickness of heave plate, and D_{Hp} is the (circumcircle) diameter of heave plate, k_3 is a shape correction factor for different heave plate cross-sections, the upper bound of C_d is limited to 12 for sake of the possible infinite value by the formula. This upper limit is proposed based on the measured Cd in the reference (Lopez-Pavon and Souto-Iglesias, 2015) in which C_d is smaller than 12 in the condition with a very small thickness ratio of 0.005.

Fig. 12 shows a comparison of numerical identified and formula predicted C_a and C_d of a single octagonal heave plate with different aspect ratios. With consideration of the shape factor $k_2 = 0.95$, predicted C_a from the present formula matches well with that obtained from the numerical simulation as shown in Fig. 12(a). As can be found from Fig. 12(b), aspect ratio dependence of C_d is also represented well by the present formula, especially for smaller aspect ratios where the unidirectional vortex shedding occurs as discussed in section 3.3. The proposed formula overestimates the drag coefficient in the transition regime in which complex interactive vortex shedding is expected. As approaching independent vortex shedding pattern, the accuracy of proposed formula for C_d improves as shown in Fig. 12(b).

Fig. 13 (a) and (b) show formulas predicted and measured C_a of a circular heave plate with an attached column, and a square heave plate, respectively. The proposed formulas are capable of predicting C_a precisely with a proper intercept and slope with variation in KC number for both circular plate with center column and square plate without column as seen from Fig. 13 (a) and (b).

Comparisons of formula predicted and measured C_d for the heave plate with circular and square cross-sections are presented in Fig. 14. It is found that the proposed formula shows a good prediction of C_d varying with KC number. In addition, the variation of C_d with aspect ratios is also well represented by the proposed formula as shown in Fig. 14(b).

Therefore, the proposed formulas of C_a and C_d for a single heave plate covers the application of different cross-sections and KC number, and show a good agreement with the measurement and present numerical results.

4.2. Added mass and drag coefficient for double heave plates

The double heave plates could provide much more added mass and damping than that of a single heave plate. The spacing (L) between the adjacent double heave plates is one key parameter in the determination of hydrodynamic coefficients. If the spacing between the two heave plates reduces to zero, the double heave plates actually act as a single heave plate. In this case, Eq. (24) and Eq. (28) can be used for evaluation of C_a and C_d, respectively. On the other hand, when the spacing exceeds a critical value, C_a and C_d will be independent of the spacing ratio. In other words, each heave plate will act as a fully separated plate. When the spacing is between zero and the critical value, a flow interaction between the double heave plates occurs, and the hydrodynamic coefficients will be dependent on the spacing ratio in this range. Therefore, the effect of spacing on the change of C_a and C_d for each heave plate should be considered.

The Hp-2 in Fig. 1 is attached by only one column, the formula of C_a is exactly the same as that for the single heave plate if the spacing exceeds a critical value. When the interaction between double heave plate occurs, the formula of C_a is derived by mathematically subtracting the intersection part of the two ellipsoids above Hp-2. The formula of C_a for Hp-2 is expressed as follows:

$$C_{a,Hp\text{-}2} = \begin{cases} k^3 - \frac{1}{32}\left[12\pi r_d^2 r_L + (2k - \pi r_L)^2(4k + \pi r_L)\right]; & r_L \le 2k/\pi \\ k^3 - \frac{1}{4}\left[3r_d^2\sqrt{k^2 - r_d^2} + \left(k - \sqrt{k^2 - r_d^2}\right)^2\left(2k + \sqrt{k^2 - r_d^2}\right)\right]; & r_L > 2k/\pi \end{cases} \tag{30}$$

where, $r_d = D_c/D_{Hp}$, $r_L = L/D_{Hp}$, and k refers to the correction factor and is given in Eq. (25).

The Hp-1 in Fig. 1 is attached by two columns at both upper and lower surfaces. Therefore, the volume taken by those two columns should be excluded. In addition, the spacing effect on the lower surface of Hp-1 should be considered. It is assumed that the upper surface of Hp-1 is sufficiently far away from the still water level. The formula of C_a for Hp-1 is expressed as follows:

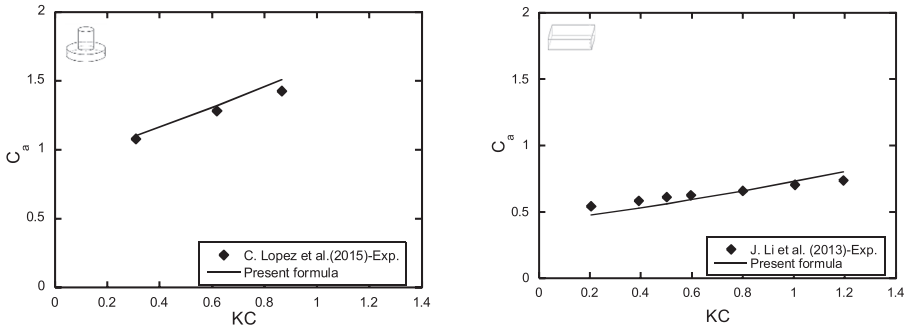

(a) Circular heave plate with a column (b) Square heave plate without a column

Fig. 13. Comparison of formula predicted and measured added mass coefficients for the single heave plates with different cross sections and KC number.

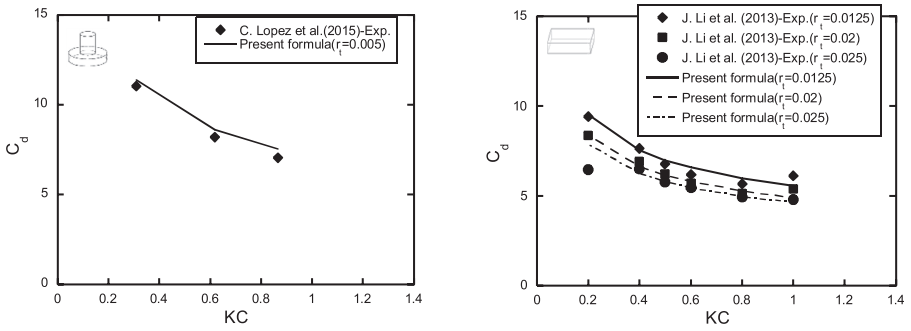

(a) Circular heave plate with a column (b) Square heave plate without a column

Fig. 14. Comparison of formula predicted and measured drag coefficients for the single heave plate with different cross sections, KC number, and aspect ratios.

$$C_{a,Hp\text{-}1}=\begin{cases} k^3-\dfrac{1}{4}\left[3r_d^2\sqrt{k^2-r_d^2}+\left(k-\sqrt{k^2-r_d^2}\right)^2\left(2k+\sqrt{k^2-r_d^2}\right)\right] \\ \quad -\dfrac{1}{32}\left[12\pi r_d^2 r_L+(2k-\pi r_L)^2(4k+\pi r_L)\right];\quad r_L\le 2k/\pi \\ k^3-\dfrac{1}{2}\left[3r_d^2\sqrt{k^2-r_d^2}+\left(k-\sqrt{k^2-r_d^2}\right)^2\right. \\ \quad \left.\left(2k+\sqrt{k^2-r_d^2}\right)\right];\quad r_L> 2k/\pi \end{cases} \tag{31}$$

As mentioned in section 3.2, C_d mainly comes from the vortex shedding around the sharp edges of heave plate. Thus, C_d of the heave plate does not depend on the number of attached columns. In addition, it is assumed that C_d linearly decreases as spacing ratio decreases. Formula of C_d for each heave plate is given as follows:

$$C_{d,Hp\text{-}i}=\begin{cases} \min\left\{1.7r_{t,Hp\text{-}i}^{-1/3.7}(KC)^{-1/k_3}-1.85k_2 \right. \\ \quad \left. +1.45r_L,\ 12\right\};\quad r_L\le 2k_2/\pi \\ \min\left\{1.7r_{t,Hp\text{-}i}^{-1/3.7}(KC)^{-1/k_3},12\right\};\quad r_L> 2k_2/\pi \end{cases} \tag{32}$$

where, $r_{t,Hp\text{-}i}$ refers to the aspect ratio of each heave plate, i.e. Hp-1 or Hp-2; k_2 and k_3 refer to the shape correction factors defined in Eq. (27) and Eq. (29). The coefficient with respect to the spacing ratio and the shape correction factor are identified according to the numerically predicted C_d in this study.

Fig. 15 shows the numerically identified and formulas predicted C_a and C_d for each heave plate with different spacing ratios. As shown in Fig. 15(a), variation of C_a with the spacing ratios is represented well by the present formula for Hp-2. Predicted C_a for Hp-1 is slightly smaller than that of Hp-2, and it is overestimated compared with the numerical identified C_a, which is due to the effect of the upper hull above Hp-1 as shown in Fig. 1. It is found that variation of C_d with the spacing ratio and effect of the aspect ratio are favorably represented by the present formula as shown in Fig. 15(b).

Fig. 16 presents numerically identified and formulas predicted C_a and C_d for each heave plate with various diameter ratios. The present formula shows a good performance for the prediction of C_a varying with the diameter ratios, especially for Hp-2. In the case of smaller diameter ratio, the gap of C_a between Hp-1 and Hp-2 is larger compared with that in the larger diameter ratio, which is due to the influence of the number of the attached column. The formula predicted C_a for Hp-1 is also overestimated, which is due to the effect of the upper hull above Hp-1 as shown in Fig. 1. In contrast to the C_a, formula predicted C_d is independent of diameter ratio, and agrees reasonably well with numerical results in this study.

The proposed formulas of C_a and C_d for each plate simultaneously consider the effects of spacing ratio, diameter ratio, aspect ratio, and KC number and show favorable agreement with the numerical simulations.

In order to evaluate C_a and C_d of double heave plates as a whole, the formulas for each heave plate can be simply summed up. As a result, integral C_a of double heave plates is obtained according to Eq. (30) and Eq. (31) as follows:

$$C_a=\begin{cases} 2k^3-\dfrac{1}{4}\left[3r_d^2\sqrt{k^2-r_d^2}+\left(k-\sqrt{k^2-r_d^2}\right)^2\left(2k+\sqrt{k^2-r_d^2}\right)\right] \\ -\dfrac{1}{16}\left[12\pi r_d^2 r_L+(2k-\pi r_L)^2(4k+\pi r_L)\right];\quad r_L\le 2k/\pi \\ 2k^3-\dfrac{3}{4}\left[3r_d^2\sqrt{k^2-r_d^2}+\left(k-\sqrt{k^2-r_d^2}\right)^2\right. \\ \left.\left(2k+\sqrt{k^2-r_d^2}\right)\right];\quad r_L> 2k/\pi \end{cases} \tag{33}$$

where, $r_d=D_c/D_{Hp}$, $r_L=L/D_{Hp}$, and k refers to the correction factor and

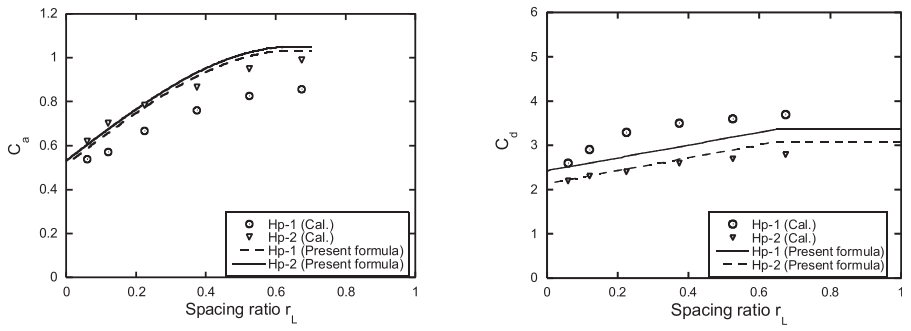

(a) Added mass coefficient (b) Drag coefficient

Fig. 15. Comparison of numerically identified and formulas predicted added mass and drag coefficients for each fully submerged plate with different spacing ratios.

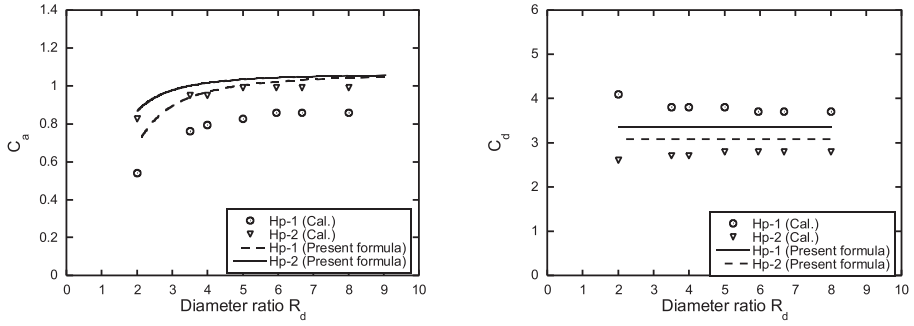

(a) Added mass coefficient (b) Drag coefficient

Fig. 16. Comparison of numerically identified and formulas predicted added mass and drag coefficients for each fully submerged plate with different diameter ratios.

is given in Eq. (25).

Similarly, formula for C_d of double heave plates is obtained as follows:

$$C_d = \begin{cases} \min\left\{1.7\left(r_{t,Hp\text{-}1}^{-1/3.7} + r_{t,Hp\text{-}2}^{-1/3.7}\right)(KC)^{-1/k_3} \\ -3.7k_2 + 2.9r_L,\ 24\right\}; \quad r_L \le 2k_2/\pi \\ \min\left\{1.7\left(r_{t,Hp\text{-}1}^{-1/3.7} + r_{t,Hp\text{-}2}^{-1/3.7}\right)(KC)^{-1/k_3},\ 24\right\}; \\ r_L > 2k_2/\pi \end{cases} \tag{34}$$

where, $r_{t,Hp\text{-}1}$ and $r_{t,Hp\text{-}2}$ represent the aspect ratio of heave plate Hp-1 and Hp-2, respectively; k_2 and k_3 refer to the shape correction factors defined in Eq. (27) and Eq. (29), respectively.

Fig. 17 shows numerically identified C_a of a double circular heave plates with different spacing ratios studied by Tao et al. (2007). C_a predicted according to the formula proposed by Tao et al. and from present formula are shown in the figure as well. It is found that C_a is strongly dependent of conducted KC number. Comparing with previous formula, the proposed formula successfully captures the trend of C_a varying with KC number. The differences between C_a predicted by the proposed formula and the numerical simulations in smaller or larger spacing ratio might be owing to the limitation of the formula in the application for the small diameter ratio. The diameter ratio of the model in the literature (Tao et al., 2007) is only 1.31, and the local flow induced by flow separation and vortex shedding might be significantly impacted by the side wall of attached column.

Fig. 18 and Fig. 19 show C_a and C_d of the octagonal double heave plates varying with spacing ratios and diameter ratios, respectively. The overestimation of C_a for Hp-1 by proposed formula leads to the over-prediction shown in Fig. 18(a). The proposed formulas in this study are suitable for the heave plates which are sufficiently far away from the still water level. The formula of C_d for double heave plates shows a good accuracy even though proposed formula show some differences in estimation of C_d for each heave plate.

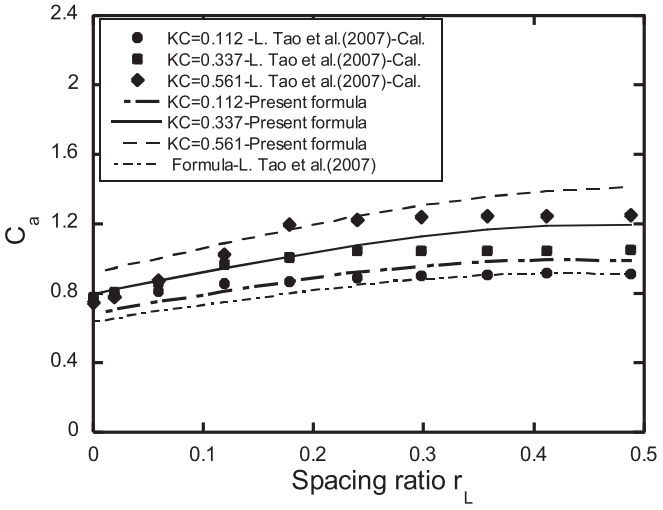

Fig. 17. Comparison of numerically identified and formulas predicted added mass coefficient as a function of spacing ratio for the double heave plates with circular cross-section studied by Tao et al. (Tao et al., 2007).

In the application of multi-plates containing more than two heave plates, the integral C_a and C_d can be evaluated according to the arrangement of the heave plates and proposed formulas for each heave plate in this study.

5. Conclusions

In this study, hydrodynamic coefficients of multiple heave plates are investigated by numerical simulations and water tank tests. The conclusions are summarized as follows:

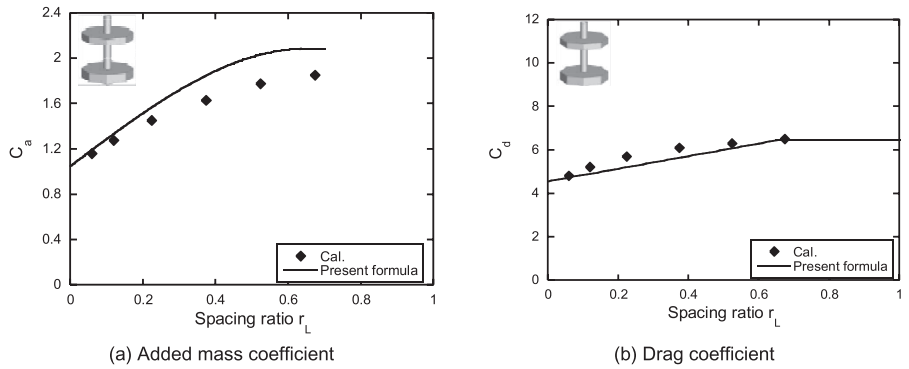

(a) Added mass coefficient (b) Drag coefficient

Fig. 18. Comparison of numerically identified and formulas predicted added mass and drag coefficients for double octagonal heave plates with different spacing ratios.

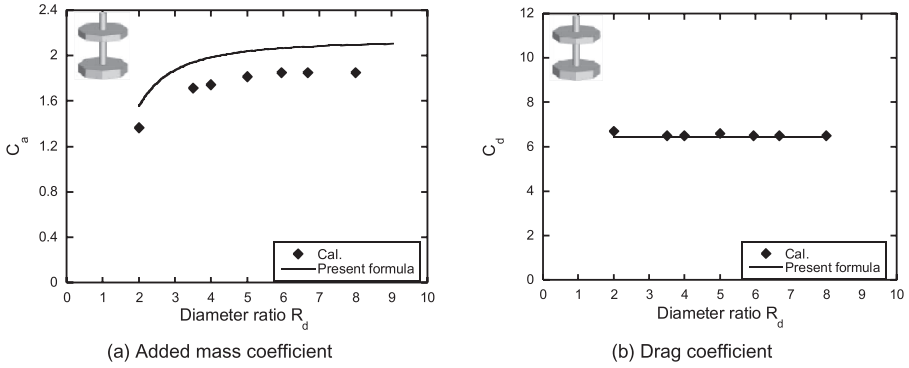

(a) Added mass coefficient (b) Drag coefficient

Fig. 19. Comparison of numerically identified and formulas predicted added mass and drag coefficients for double octagonal heave plates with different diameter ratios.

1. Added mass and drag coefficients of multiple heave plates predicted by large eddy simulations with volume of fluid method show a good agreement with the experimental data by the water tank test. Grid and time step dependencies are investigated. Fine grid and small time step are required to accurately simulate the unsteady flow separation around the sharp edges of the heave plates, which affect the accuracy of predicted drag coefficient.
2. Effects of spacing ratio and diameter ratio of the multiple heave plates are systematically studied by large eddy simulations. The added mass coefficient, C_a, increases as the spacing ratio increases till a critical value of spacing ratio and also increases as the diameter ratio increases. The drag coefficient, C_d, increases as the spacing ratio increases and is independent of the diameter ratio. For a single heave plate, C_a is independent of the aspect ratio, but C_d decreases rapidly as the aspect ratio increases and it approaches a constant value when the aspect ratio exceeds a critical value.
3. Shape correction factors are proposed in the formulas of C_a and C_d for a single plate and double heave plates. The formulas for a single heave plate with different cross-sections are validated by the data in the literature and the numerical simulations. In addition, formulas of C_a and C_d for each heave plate in the double heaves are also proposed and validated by the numerical simulations in this study.

Acknowledgement

This research is carried out as a part of the Fukushima floating offshore wind farm demonstration project funded by the Ministry of Economy, Trade and Industry (gs:_501100003050). The authors wish to express their deepest gratitude to the concerned parties for their assistance during this study.

References

An, S., Faltinsen, O.M., 2013. An experimental and numerical study of heave added mass and damping of horizontally submerged and perforated rectangular plates. J. Fluids Struct. 39, 87–101.
Browning, J., Jonkman, J., Robertson, A., Goupee, A., 2014. Calibration and validation of a spar-type floating offshore wind turbine model using the FAST dynamic simulation tool. In: Journal of Physics: Conference Series. IOP Publishing.
Fluent Theory Guide, 2012. Ansys Inc., Canonsburg, PA.
Fukushima FORWARD: http://www.fukushima-forward.jp/english/index.html.
Garrido-Mendoza, C.A., Thiagarajan, K.P., Souto-Iglesias, A., Colagrossi, A., Bouscasse, B., 2015. Computation of flow features and hydrodynamic coefficients around heave plates oscillating near a seabed. J. Fluids Struct. 59, 406–431.
GOTO FOWT:http://goto-fowt.go.jp/english/.
Graham, J., 1980. The forces on sharp-edged cylinders in oscillatory flow at low Keulegan–Carpenter numbers. J. Fluid Mech. 97 (02), 331–346.
Holmes, S., Bhat, S., Beynet, P., Sablok, A., Prislin, I., 2001. Heave plate design with computational fluid dynamics. J. Offshore Mech. Arct. Eng. 123 (1), 22–28.
Hywind Demo: http://innovate.statoil.com/challenges/hywind/Pages/default.aspx.
Jonkman, J.M., 2007. Dynamics Modeling and Loads Analysis of an Offshore Floating Wind Turbine. ProQuest.
Kvittem, M.I., Bachynski, E.E., Moan, T., 2012. Effects of hydrodynamic modelling in fully coupled simulations of a semi-submersible wind turbine. Energy Procedia 24, 351–362.
Li, J., Liu, S., Zhao, M., Teng, B., 2013. Experimental investigation of the hydrodynamic characteristics of heave plates using forced oscillation. Ocean. Eng. 66, 82–91.
Lopez-Pavon, C., Souto-Iglesias, A., 2015. Hydrodynamic coefficients and pressure loads on heave plates for semis-submersible floating offshore wind turbines: a comparative analysis using large scale models. Renew. Energy 81, 864–881.
Oka, S., Ishihara, T., 2009. Numerical study of aerodynamic characteristics of a square prism in a uniform flow. J. Wind Eng. Industrial Aerodynamics 97 (11), 548–559.
Philip, N.T., Nallayarasu, S., Bhattacharyya, S., 2013. Experimental investigation and CFD simulation of heave damping effects due to circular plates attached to spar hull. Ships Offshore Struct. 1–17.
Phuc, P.V., Ishihara, T., 2007. A Study on the Dynamic Response of a Semi-submersible Floating Offshore Wind Turbine System Part 2. numerical simulation. ICWE12, Cairns, Australia, pp. 959–966.
Prislin, I., Blevins, R.D., Halkyard, J.E., 1998. Viscous Damping and Added Mass of a Square Plate. OMAE98–316., Lisbon, Portugal.

Sarpkaya, T., 2010. Wave Forces on Offshore Structures. Cambridge University Press.
Stern, F., Wilson, R.V., Coleman, H.W., Paterson, E.G., 2001. Comprehensive approach to verification and validation of CFD simulations - Part 1: methodology and procedures. Trans. ASME 123, 793–802.
Tao, L., Cai, S., 2004. Heave motion suppression of a Spar with a heave plate. Ocean. Eng. 31 (5), 669–692.
Tao, L., Dray, D., 2008. Hydrodynamic performance of solid and porous heave plates. Ocean. Eng. 35 (10), 1006–1014.
Tao, L., Thiagarajan, K., 2003. Low KC flow regimes of oscillating sharp edges. II. Hydrodynamic forces. Appl. ocean Res. 25 (2), 53–62.
Tao, L., Thiagarajan, K., 2003. Low KC flow regimes of oscillating sharp edges I. Vortex shedding observation. Appl. ocean Res. 25 (1), 21–35.
Tao, L., Lim, K.Y., Thiagarajan, K., 2004. Heave response of classic spar with variable geometry. J. Offshore Mech. Arct. Eng. 126 (1), 90–95.
Tao, L., Molin, B., Scolan, Y.-M., Thiagarajan, K., 2007. Spacing effects on hydrodynamics of heave plates on offshore structures. J. Fluids Struct. 23 (8), 1119–1136.
Wadhwa, H., Thiagarajan, K.P., 2009. Experimental assessment of hydrodynamic coefficients of disks oscillating near a free surface. In: ASME 2009 28th International Conference on Ocean, Offshore and Arctic Engineering. American Society of Mechanical Engineers.
Wadhwa, H., Krishnamoorthy, B., Thiagarajan, K.P., 2010. Variation of heave added mass and damping near seabed. In: ASME 2010 29th International Conference on Ocean, Offshore and Arctic Engineering. American Society of Mechanical Engineers.
Waris, M.B., Ishihara, T., 2012. Dynamic response analysis of floating offshore wind turbine with different types of heave plates and mooring systems by using a fully nonlinear model. Coupled Syst. Mech. 1 (3), 247–268.
WindFloat:http://windfloatpacific.com/.
Yang, J., Tian, X., Li, X., 2014. Hydrodynamic characteristics of an oscillating circular disk under steady in-plane current conditions. Ocean. Eng. 75, 53–63.
Yoshimoto, H., 2016. The Validation of the Motion Performance of the Advanced Spar Type Floater. WWEC15, Tokyo, Japan.